Advances in Biological Regulation xxx (xxxx) xxx

Contents lists available at ScienceDirect

Advances in Biological Regulation

journal homepage: www.elsevier.com/locate/jbior

Comparison of extracellular vesicles and mechanically induced vesicles for structural determination of membrane proteins

Chunyang Wang [a], Ole Østergaard [b,c], Roberto Melero [d], Gabriela Nagy-Davidescu [a], Matthias Eibauer [a], Jesper Velgaard Olsen [b,c,*], Jose Maria Carazo [d,**], Andreas Plückthun [a,***], Ohad Medalia [a,****]

[a] Department of Biochemistry, University of Zurich, Winterthurerstrasse 190, 8057, Zurich, Switzerland
[b] Novo Nordisk Foundation Center for Protein Research, Faculty of Health and Medical, Denmark
[c] Copenhagen Center for Glycocalyx Research, Department of Cellular and Molecular Medicine, Faculty of Health and Medical Sciences, University of Copenhagen, Denmark
[d] Instruct Image Processing Center, National Center of Biotechnology, 28049, Madrid, Spain

ARTICLE INFO

Handling Editor: Dr. L. Cocco

ABSTRACT

The structural and functional characteristics of membrane proteins can be influenced by the composition of the membrane. Consequently, native membranes are most relevant for the study of receptors and other membrane proteins. In this study, we investigated two types of cell-derived vesicles: natively shed extracellular vesicles (EVs) and mechanically derived vesicles (MVs). To this end, we utilized the human breast cancer cell line SKBR3, which strongly overexpresses the receptor HER2. We designed a protocol based on designed ankyrin repeat proteins (DARPins) to purify EVs and MVs enriched in HER2, and to ensure the native orientation of the HER2 receptors within the vesicle. The isolated HER2-containing EVs and MVs were characterized by cryogenic electron microscopy (cryo-EM), cryo-electron tomography (cryo-ET) and mass spectrometry (MS), which revealed fundamental differences between the different vesicle types. Our study highlights the greater structural diversity of EVs over MVs. A single particle cryo-EM analysis and classification of all visible receptors on the vesicle surface yielded electron density consistent with HER2 at modest resolution. Taken together, our results suggest that MVs can provide a more suitable platform than EVs for the structural determination of membrane proteins within their native membrane environments.

This article is part of a special issue entitled: Symposium issue 2026 published in Advances in Biological Regulation.

* Corresponding author. Copenhagen Center for Glycocalyx Research, Department of Cellular and Molecular Medicine, Faculty of Health and Medical Sciences, University of Copenhagen, Denmark.
** Corresponding author.
*** Corresponding author.
**** Corresponding author.
E-mail addresses: jesper.olsen@cpr.ku.dk (J.V. Olsen), carazo@cnb.csis.es (J.M. Carazo), plueckthun@bioc.uzh.ch (A. Plückthun), omedalia@bioc.uzh.ch (O. Medalia).

https://doi.org/10.1016/j.jbior.2026.101191
Received 2 September 2026; Received in revised form 11 November 2026; Accepted 11 November 2026
Available online 14 November 2026
2212-4926/© 2026 The Authors. Published by Elsevier Ltd. This is an open access article under the CC BY license (http://creativecommons.org/licenses/by/4.0/).

Please cite this article as: Chunyang Wang et al, *Advances in Biological Regulation,* https://doi.org/10.1016/j.jbior.2026.101191

1. Introduction

Membrane proteins are essential for cellular function because they are involved in many fundamental processes such as cell signalling, solute transport, immune responses, and synaptic transmission. Previous studies have shown that the local membrane environment intricately controls many aspects of membrane protein properties (Harayama and Riezman, 2018; Levental and Lyman, 2023). For example, membrane lipid composition is coupled to protein conformational changes (Bechara et al., 2015; Vitrac et al., 2013), the membrane environment influences protein diffusion (Munguira et al., 2016), and the interactions between co-localized proteins in the same membrane contribute to cell signalling (Cheng and Smith, 2019). Therefore, the structure of a membrane protein would ideally be determined in its native membrane environment.

Structural determination of membrane proteins currently relies on overexpression systems (Kesidis et al., 2020) and the subsequent isolation of the proteins of interest in detergents, optionally their incorporation into synthetic lipid bilayers (Denisov and Sligar, 2016; Rouck et al., 2017). These approaches provided unprecedented information expanding our understanding of how membrane proteins function. However, the native membrane environment is lost during such sample preparations. Cryo-electron tomography (Cryo-ET) combined with focused ion beam (FIB) milling has emerged as a promising method for studying the structures of biological molecules in their native cellular environments (Harapin et al., 2015; Keller and Fernandez-Busnadiego, 2024; Mahamid et al., 2016; Schaffer et al., 2017). However, due to the dense molecular crowding in membranes, the small size of many membrane proteins and the low signal-to-noise ratio of cryo-ET, the structural features of many membrane proteins are challenging to interpret and/or too weak to be clearly identified and determined. As a result, this method is primarily limited to studying very large membrane-associated protein complexes, such as membrane attached ribosomes (Englmeier et al., 2017) or nuclear pore complexes (Schuller et al., 2021; Zimmerli et al., 2021).

Cell-derived membrane vesicles have emerged as promising platforms for studying membrane proteins in a near-native environment (Delauzun et al., 2020; Han et al., 2019; Kaplan et al., 2016; Rubinstein, 2026; Zeev-Ben-Mordehai et al., 2014). Different types of membrane vesicles can be obtained, depending on the experimental procedure. For example, extracellular vesicles (EVs) are a heterogeneous group of membrane vesicles naturally released from cells (Banerjee et al., 2023; Tkach and Thery, 2016; van Niel et al., 2018). Different functions of EVs were considered, such as the selective elimination of proteins, lipids and nucleic acids from cells, as well as intercellular communication through the transfer of bioactive constituents from one cell to the other (Kalluri and McAndrews, 2023; van Niel et al., 2018). Another type of vesicle is mechanically induced membrane vesicles (MVs), also denoted cell-derived vesicles and a variety of other names (Lau et al., 2022). MVs can be generated by extruding cells through a syringe (Goh et al., 2017; Jang et al., 2013; Lau et al., 2022). They contain many of the original cellular lipids and membrane proteins, often in their original composition (Kaplan et al., 2016; Levental et al., 2011). While different types of cell-derived membrane vesicles have already been used to investigate the structure of membrane proteins (Rubinstein, 2026; Tao et al., 2023; Zeev-Ben-Mordehai et al., 2014), these studies were still built on protein over-expression procedures.

HER2 is a member of the epidermal growth factor receptor (EGFR) family of receptors (Yarden and Sliwkowski, 2001). Overexpression of HER2 has been implicated in the development and progression of tumours and is commonly associated with aggressive forms of breast and gastric cancers. HER2 is the preferred dimerization partner of members from the EGFR family of receptors. As HER2 has no known ligand, it is thought to adopt the extended conformation that would be able to dimerize with other EGFR members (Graus-Porta et al., 1997). However, HER2 can adopt a cluster of conformations and when highly overexpressed such as in several forms of cancers, it can heterodimerize even in the absence of a ligand of the other receptor (Junttila et al., 2009).

HER2 is a prime candidate for tumour-targeting therapeutics, since ~20-30% of breast cancers and ~20% of gastric cancers show HER2 overexpression, usually correlated with rapid disease progression and poor survival rates (Nabholtz et al., 2002). Over the last few decades, small-molecule tyrosine kinase inhibitors (TKIs) (Shyam Sunder et al., 2023) and humanized monoclonal antibodies (mAbs) (Costa and Czerniecki, 2020) have been developed to target HER2-positive cancers. While kinase inhibitors have resulted in low clinical efficacies during clinical trials (Liu et al., 2023; Saifudeen et al., 2026), probably because selection pressure leading to kinase mutations renders the inhibitor inactive, anti-HER2 mAbs have become an integral part of the standard of care for HER2-positive breast cancers. Indeed, combined therapies of mAbs with chemotherapy have turned out to be most efficacious in treating HER2-positive breast cancer (Bhagyalalitha et al., 2024), and anti-HER2 antibody drug conjugates (ADCs) are being clinically used now as well (Yu et al., 2022).

Here, we set out to evaluate possible approaches to generate HER2-enriched vesicles. To this end, we used SKBR3 cells, a HER2-overexpressing human breast cancer cell line (Chung et al., 2016). Two types of cell-derived vesicles were produced and compared: spontaneously released EVs and mechanically induced MVs. Using an affinity purification strategy based on designed ankyrin repeat proteins (DARPins) (Pluckthun, 2015) immobilized on magnetic beads and cleavable by a specific protease, we successfully enriched HER2-containing vesicles. Cryo-ET and mass-spectrometry were employed to analyze the structure and composition of the vesicles, the crowdedness of their surface, and their membrane protein distributions. Finally, we applied cryo-EM on purified MVs to reconstruct receptor structures on the vesicle surface.

2. Materials and methods

2.1. Cell culture

SKBR3 cells and CHO cells were cultured in Roswell Park Memorial Institute (RMPI) 1640 medium (GibcoTM, 21875-034) containing 10% (v/v) Foetal Calf Serum (FCS) (BioConcept, 2-01F10-I) and 1% (v/v) penicillin-streptomycin (Sigma-Aldrich, P0781) at

37°C and 5% CO_2. For fluorescence analysis, the cultured cells were first detached with 1x trypsin-EDTA solution (Sigma-Aldrich, T4174) and then seeded onto a 35-mm cell culture dish with glass bottom (MatTek, P35G-1.5-14-C) and grown overnight.

2.2. EVs and MVs vesicle preparation and purification

To prepare extracellular vehicles (EVs), 10 × 15 cm cell dishes of cultured SKBR3 cells at ~80% confluency grown in serum-free RMPI 1640 medium overnight. The spent medium was collected (~200 mL), and cells and debris were removed by centrifugation at 2000 × g for 10 min. The supernatants were then filtered using 0.8 μm filters (Sartorius Stedium Biotech GmbH) before concentration with Amicon Ultra - 15 centrifugal filters (10 kDa) to reduce the volume to ~10 mL. EVs were pelleted by centrifugation at 4°C for 30 min at 20,000 × *g*. The supernatants were carefully removed and 1 mL of PBS was added for resuspending the EVs, which were then pelleted again. The enriched EVs were suspended in 20 μL PBS for characterization.

To prepare mechanically induced vesicles (MVs), the SKBR3 cells were manually detached using a cell scraper, spun down at 1000 × g for 10 min and resuspended with homogenization buffer (20 mM Tris pH 7.4, 1 mM EDTA and 250 mM sucrose), supplemented with phosphatase inhibitors and a protease inhibitor cocktail (Complete Mini, Roche). Each sample was passed multiple times through a Syringe (27G × 1½, 0.4 mm × 40 mm), the cells were broken and vesicles were generating from the cells. Subsequently, the unbroken cells and cell debris were removed by centrifugation at 1000 × g for 10 min followed by centrifugation of the supernatant at 10,000 × g for 50 min at 4°C. The membrane vesicles were then collected at 110,000 × g for 1 h at 4°C and resuspended in 20 mM HEPES (pH 7.4) for characterization.

2.3. Specific binding of DARPin G3 coated magnetic beads to HER2 expressing cells

SKBR3 cells and CHO cells—not expressing HER2—were cultured in 12-well cell culture plates. Aliquots of 10 μL magnetic beads were coated (see next section) with DARPin G3 or E3-5 (with no measurable affinity for HER2 as a control) prior to incubation with cells, in 1 mL serum-free RPMI 1640 medium for 1 h. To avoid bead sedimentation, the cell plates were gently shake at 100 rpm/min. Then the cells were washed 3 times for 10 min with a higher shaking speed of 200 rpm/min. Light microscopy images were acquired to verify the specificity of the binding.

2.4. Enrichment of HER2-positive vesicles using magnetic beads

To enrich for vesicles that expose the extracellular domain of HER2, HER2 binding DARPins with a 3C cleavage site (described below) were coupled to magnetic beads for vesicle enrichment. The 3C cleavage site enabled easy release of the vesicles by addition of the 3C protease.

The DARPin G3 (abbreviated as G3) (Zahnd et al., 2007) was fused with an N-terminal MRGS-His_6 tag and a C-terminal Avi-tag preceded by a 3C protease cleavage site (LEVLFQGP). G3 was expressed and purified as described previously (Zahnd et al., 2007). The DARPins were biotinylated in vitro using biotin ligase and purified using Nickel-NTA and gel filtration chromatography. The protein concentration of purified biotinylated DARPin G3 was 294 μM, evaluated with a Nanodrop 2000 Spectrophotometer (Thermo Scientific) at 280 nm.

The biotinylated DARPin G3 was then immobilized on streptavidin-coated magnetic beads. For each experiment, 10 μL of G3 were incubated with 200 μL Dynabeads™ Biotin Binder (Invitrogen™, 11047) for 1 h, at 4°C. After 3 washes (10 min) with 20 mM HEPES 1% BSA, the G3-coated beads were incubated with SKBR3 cell-derived vesicles for 1 h at 4°C. Then the beads were washed three times with 20 mM HEPES buffer to remove unbound vesicles and pelleted by a homemade weak magnet to minimize bead aggregation. After the first two washes, the beads were resuspended in 20 mM HEPES with 1% BSA, and after a third washing step, the beads were resuspended in 20 mM HEPES without BSA. Vesicles were then released from the beads by addition of 4 μL 3C protease (GenScript, Z03092) followed by incubation for 2 h at 4°C. The supernatant was collected and concentrated using a Vivaspin-500 filter (100 kDa, Sartorius, VS0141) to ~10 μL for cryo-EM analysis. For the control experiment, a HER2-non-binding DARPin (E3-5) was used at 241 μM, and the 11 μL of E3-5 in the same format was used for immobilization on magnetic beads in each individual experiment.

2.5. Immunofluorescence and confocal microscopy

Cells cultured on coverslips were fixed using 3.7% paraformaldehyde (4 min) and then permeabilized with 0.1% Triton X-100 (Sigma-Aldrich, T8787) for 10 min prior to incubation with blocking buffer (2% w/v BSA, 22.5 mg/mL glycine in PBS, pH 7.5, supplemented with 0.1% Tween-20 (PBST)) for 1 h at room temperature. The primary anti-HER2 antibody 3B5 (Merck, MABE330, 1:1000) was diluted in blocking buffer and incubated with the cells overnight at 4°C. After 3 washes with PBST, the FITC-labeled secondary antibody (Jackson ImmunoResearch, 715-095-150, 1:200) was applied for 1 h at room temperature. Cell nuclei were stained with Hoechst 33342 (Sigma-Aldrich, B2261) at room temperature for 30 min. The samples were then further washed (3 × 10 min) with PBS. HER2 localization was recorded in the GFP channel, and the Hoechst channel was recorded to visualize nuclei. The fluorescence images were acquired using a DMI4000B microscope (Leica Microsystems), and confocal scanning microscopy images were acquired with a Leica SP8 inverse FALCON laser scanning microscope. 3D stacks were reconstructed in Imaris 9.6.0.

2.6. Mass spectrometry analysis of vesicle samples

2.6.1. NTA measurements

Vesicle samples with EVs and MVs were analyzed by nanoparticle tracking analysis (NTA) using a Zeta View PMX-220 NTA analyzer (Particle Metrix, Germany) equipped with a 520 nm laser to estimate the particle concentrations. In brief, samples were diluted 1:10,000 with PBS then, from this dilution, 1 mL was injected into the NTA analyzer and nanoparticles were counted by scanning at 11 different locations twice at 22°C. The recorded data were analyzed and summarized using the ZetaView software version 8.05.14 SP7 reporting vesicle concentrations in the original samples.

2.6.2. OneTip sample digestion and desalting

For tryptic protein digestion prior to analysis by mass spectrometry, EV and MV samples were digested directly on EvoTips, essentially as described (Ye et al., 2024). In brief, samples were diluted to 10^7 particles/μL. Five μL of diluted sample was then loaded on EvoTips which were prepared as follows: First, tips were rinsed with 20 μL 80% acetonitrile, 0.1% TFA, then soaked with isopropanol, followed by a step to equilibrate the C18 material by loading 20 μL 0.1% formic acid. After each step, the reagent was removed by gentle centrifugation of the tips in the EvoTip box at 600 x g for 60 s. The equilibrated tips were then supplied with 5 μL digestion mix (100 mM triethyl-ammonium bicarbonate, 0.2% n-dodecyl-β-D-maltoside (DDM), 20 ng/μL Trypsin, and 10 ng/μL endo-LysC) before adding 5 μL of sample with EVs or MVs. Mixing was ensured by centrifugation for a few seconds at 50 x g before incubation at 37°C in an EvoTip box filled with just enough water to ensure that the C18 part of the EvoTips were immersed into the water. After 4 h, 50 μL 0.1% formic acid were added to the EvoTips followed by centrifugation 60 s at 600 x g. Then the tips were desalted by washing with 20 μL 0.1% formic acid before adding 100 μL 0.1% formic acid and placement in an EvoTip box for running the sample using an EvoSep One system.

2.6.3. Mass spectrometry analysis

Samples were eluted directly from EvoTips onto a C18 column (Aurora Rapid 75, 5 cm × 75 μm, 1.7 μm beads, IonOptics) and eluted into an Astral mass spectrometer (Thermo Fisher Scientific) using an Evosep One LC-system (Evosep, Odense, Denmark) running 16 min gradients (80 samples per day). The spray voltage was 1800 V and the ion transfer tube was 275°C. Full scan spectra (380-980 Th) were recorded at 240,000 resolution, 500% AGC, max 30 ms injection time, while MS2 spectra were recorded in a data independent acquisition mode by 149 sequential narrow windows (4 Th), max 6 ms injection time, a normalized collision energy at 25 and an RF lens set to 40%.

2.6.4. Database searching and protein quantitation

The generated raw files were searched using Spectronaut v20.2 against the SwissProt database including 20,426 human sequences downloaded on 17-10-2023) along with small FASTA files containing sequences for DARPin 9.26, streptavidin, 3C protease, trypsin and endo-lysyl endopeptidase (endo-LysC) and common contaminants from bovine serum often observed in samples from cell culture. The following settings in Spectronaut were applied: Enzyme: Trypsin/P, peptide length - min 7 AA, max 52 AA, max 2 missed cleavages; Fixed modifications - none; Variable modifications - Oxidation(M), Acetyl (Protein N-term); Protein LFQ method: MaxLFQ, Quantity level: MS2, Quantity type: Area. iBAQ values were calculated outside Spectronaut by dividing MaxLFQ quantities from Spectronaut by the *in-silico* calculated number of observable tryptic peptides with no missed cleavage sites.

2.7. Cryo-ET and cryo-EM, sample preparation and data acquisition

3 μL of vesicle samples were applied to glow-discharged holey carbon copper EM grids (R2/1, 200 mesh, Quantifoil), followed bz the addition of 3 μL of 6 nm gold fiducial markers (Aurion). Samples were plunge-frozen into liquid nitrogen-cooled ethane using a Vitrobot (Thermo Fisher). Tilt series were acquired using a FEI Titan Krios G1 electron microscope (Thermo Fisher) equipped with a Gatan Quantum Energy Filter and a K2 Summit direct electron detector (Ametek). Data were acquired at 81k magnification, resulting in a pixel size of 0.172 nm. All tomograms were acquired at 2.5-3.5 μm underfocus, covering an angular range of ±60° with a 3° increment, and a total electron dose of ~120 $e^-/Å^2$. SerialEM was used for tomogram acquisition and IMOD (Kremer et al., 1996) was used for reconstructions of tomograms.

A total number of 37, 56, 144, and 103 tomograms were collected from the samples with EVs, HER2-enriched EVs, mechanically induced vesicles (MVs) and HER2-enriched MVs, respectively. Diameters of the vesicles were manually measured in 3dmod and analyzed in Microsoft Excel and Origin (OriginLab Corp.).

For single-particle cryo-EM, 3 μL vesicle samples were loaded on glow-discharged holey carbon gold EM grids (R2/2, 200 mesh, Quantifoil). The grids were blotted briefly, and an additional 3 μL of the vesicle sample was loaded, to increase vesicle density on the grids. All EM grids were vitrified using a manual plunger (MPI, Martinsried). The data were collected using a Titan Krios G3i (Thermo Fisher) equipped with a Gatan BioQuantum Energy Filter and a K3 Summit direct electron detector (Ametek), at a magnification of 130k, resulting in a pixel size of 0.651 Å. The micrographs were automatically acquired with an underfocus range between 1.5 and 3.2 μm using Thermo Fisher Smart EPU software with a total electron dose of ~60 $e^-/Å^2$.

2.7.1. Data quality assesment by ribosome reconstruction

Ribosomes present in the sample, enclosed by vesicle membranes, were used to confirm the sample and data quality. Image processing was performed in Scipion (de la Rosa-Trevin et al., 2016), with an initial dataset of 12,373 movies of MVs. Particle picking

was divided into two steps: manual picking of ribosomes in a few micrographs, followed by auto-picking using Xmipp. The CTF was estimated using Gctf. A total of 257,176 particles were extracted at 1.3 Å/pixel in a box-size of 400×400 pixels and used for 2D classification using CryoSPARC (Punjani et al., 2017). 87,891 particles were used for the initial model, generating a 3D map using CryoSPARC. After using non-uniform refinement in CryoSPARC, a map at 2.8 Å resolution and B-factor −45.3, was obtained. The sharpening was applied to the final map.

2.7.2. Image processing of MVs

The rationale behind the image processing pipeline was to reconstruct the structure of receptors that exhibit extracellular and cytoplasmic domains, similar to HER2. The pipeline is shown in Fig. S6.

All micrographs were imported into CryoSPARC (Punjani et al., 2017), where the Patch Motion Correction, Patch CTF Estimation, Blob Picker and Topaz Extract were used for frame alignment, CTF correction, and particle picking, respectively. After identifying all vesicles, a primary classification to remove false particles located on carbon edges or inside vesicles was used, the particles were extracted in a box size of 48 × 48 pixels with binning factor 10. For the second classification step, the particles were re-extracted with binning factor 6. The ab initio reconstruction procedure was selected for initial template creation and used for primary 3D particle alignment with non-uniform refinement. In the next step, we focused on the cytoplasmic densities of the receptor. To this end, the centre of each extracted particle was shifted to the inside of the vesicles with the volume alignment tools, and the particles were re-extracted using a box size of 34 × 34 pixels with a binning factor of 6. After 2D classification, the whole map was reconstructed with the particles extracted in a box size of 84 × 84 pixels with binning 6, while maintaining the primary alignment. In this way, we restricted the particle data to only those that exhibit also a cytoplasmic density, as expected for HER2.

The final step in the 3D reconstruction was conducted with Relion5 (Scheres, 2012). To transfer the particles from CryoSPARC (Punjani et al., 2017) to Relion5, the particles were extracted in a box size of 80 × 80 pixels with binning 3 in CryoSPARC, and then the PYTHON script csparc2star.py (Asarnow et al., 2019) was used for the conversion to the Relion format.

The 3D classification and 3D refinement were performed in Relion5. To generate a featureless 3D reference structure, the template was derived from the previous refinement map, using C20 rotational symmetry, chosen arbitrarily. Blush regularization (Kimanius et al., 2024) was used for 3D classification. The local resolution map was calculated with ResMap.

2.7.3. Molecular docking of AlphaFold models into the experimental density map

The AlphaFold2 (Jumper et al., 2021) predicted structures of full length HER2 were downloaded. The truncated structure consisting of subdomains I, II, and III was fitted to the density map using Phenix docking (Adams et al., 2010). The A lphaFold2 (Jumper et al., 2021) predicted structures of all other abundant and possible membrane protein candidates were also downloaded. According to the domain boundaries and the model confidence derived from the pLDDT score, only extracellular domains were used for docking. The models were also fitted into our experimental 3D data and the correlation coefficient was recorded in Chimera (Pettersen et al., 2004).

2.7.4. Statistical analysis

Segmentation of vesicle tomograms was conducted in the Dragonfly 3D software. Analysis of internal density of vesicles was calculated in MATLAB R2019b software using the TOM Toolbox (Nickell et al., 2005). The diameters of SKBR3 and HER2 extracellular vesicles, with or without embedded cytoskeleton, was calculated using MATLAB R2019b software, and statistical analysis and figure preparation were performed using GraphPad Prism 10 software. Differences in vesicle diameter associated with receptor type and the absence or presence of an embedded cytoskeleton was assessed using the Welch's *t*-test.

3. Results

Naturally occurring extracellular vesicles are shed from the surface of cells into the extracellular space (Banerjee et al., 2023; Tkach and Thery, 2016; van Niel et al., 2018). EVs have attracted interest because they alter the extracellular environment, participate in intercellular communication, and facilitate cell invasion through cell-independent matrix proteolysis (Schmidtmann and D'Souza-Schorey, 2023). In human plasma, platelet/derived EVs constitute the majority of the circulating vesicles found in blood (Diamant et al., 2004). In some cancer cells, EVs are enriched in EGFR (Salih et al., 2025), and they were used to reconstruct a structure of EGFR dimers (Gonzalez-Magaldi et al., 2025), although only to a modest resolution. On the other hand, mechanically induced vesicles (MVs) have been used to obtain insight into EGFR dynamics in cancer cells by NMR (Kaplan et al., 2016). More recently, mechanically induced vesicles were introduced for structural studies of overexpressed ion channels by cryo-EM (Tao et al., 2023). In the current work, we aimed to isolate and characterize the two different vesicle types, EVs and MVs in order to assess their suitability for studying the structure of natively expressed membrane receptors.

3.1. Morphological characterization of EVs and MVs derived from SKBR3 cells

SKBR3-derived EVs were harvested and purified from spent media obtained from cells grown in serum-free medium for 14 h whilst MVs were generated by passing the same cells through a syringe, a method shown to generate plasma membrane vesicles (Kaplan et al., 2016) (Fig. 1a and Methods section). To compare their suitability for structural analyses of receptors embedded in the plasma membrane, we purified EVs and MVs and subjected them to cryo-EM, cryo-ET, and mass spectrometry analysis (Fig. 1a). Low-magnification cryo-EM micrographs of the EVs and MVs showed that the preparations exhibit comparable diameter. Therefore,

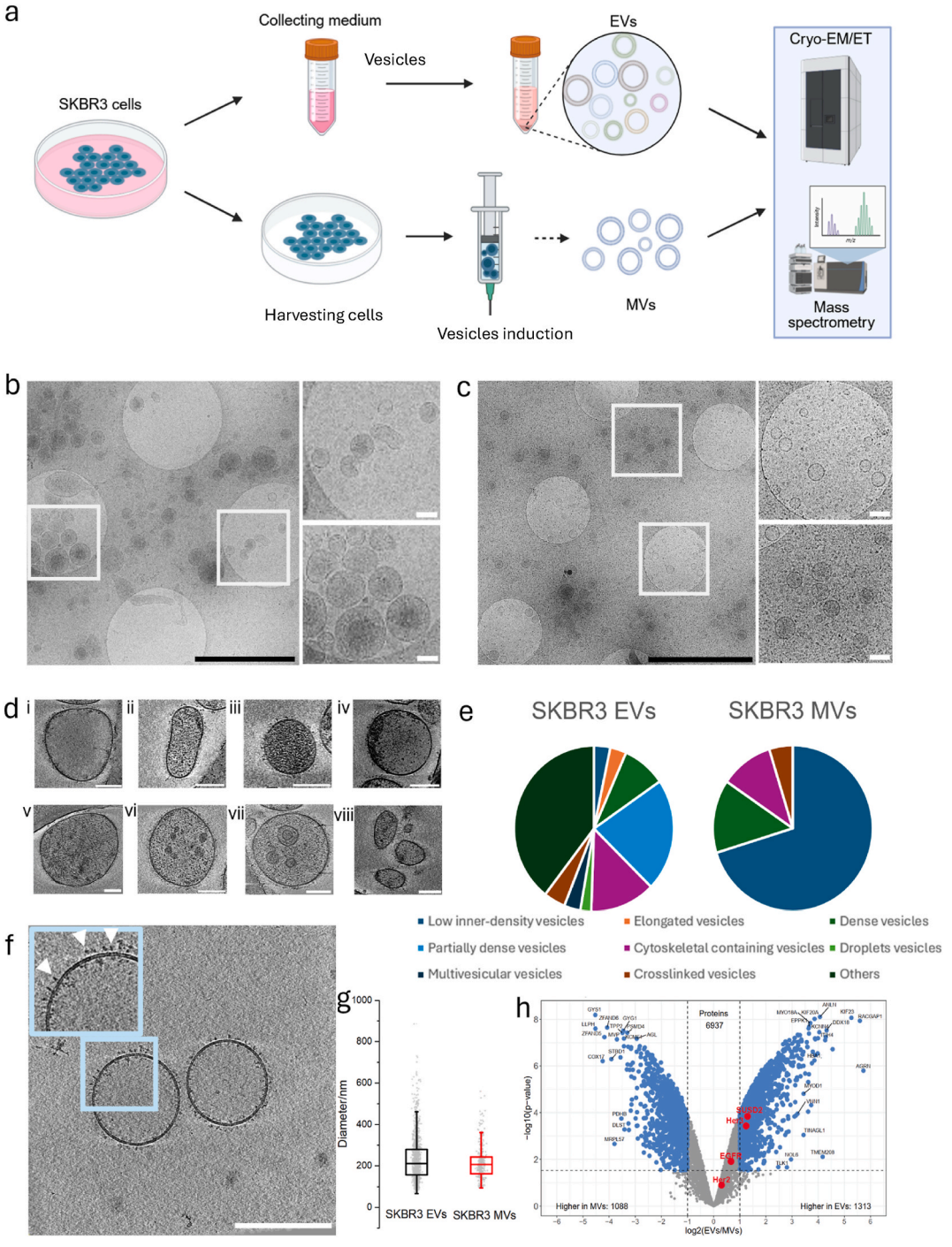

(caption on next page)

Fig. 1. SKBR3-derived EVs and MVs. a. A schematic illustration of two different types of vesicle preparations and analysis. EVs are naturally released by cells, while MVs are mechanically created by extrusion through a syringe. **b** and **c.** Representative cryo-EM micrographs of SKBR3-derived EVs and MVs respectively, indicating the comparable size of both vesicle types. White framed regions are shown at higher magnification (right). Black scale bars 2 μm. White scale bars 100 nm. **d.** SKBR3 EVs and MVs were classified into nine classes, based on their morphology. An *x-y* tomographic slice is shown for each class of vesicles, while percentages are indicated for EVs and MVs respectively: **i**-Low inner-density vesicles, 4%, 78%. **ii**-Elongated vesicles, 3%, 0%. **iii**-Dense vesicles, 9%, 8%. **iv**-Partially dense vesicles, 22%, 0%. **v**-Cytoskeleton-containing vesicles, 13%, 9%. **vi**-Droplet-containing vesicles,2%, 0%. **vii**-Multilamellar vesicles, 3%, 0% **viii**-Crosslinked vesicles, 4%, 5% and 'other vesicles' 40%, 0%. **e**. Pie diagrams showing the class distribution of EVs and MVs. The low inner-density vesicles class is the most frequent class in MVs. **f.** An x-y tomographic slice through a typical sample of SKBR3 MVs, class **i**. A higher magnification of the framed region is shown (top left), where receptors are visible (white arrowheads). **g.** The diameters distribution of both EVs and MVs are shown. No significant differences were detected, although the MVs show less variability in size. **h**. Volcano plot comparing the protein composition of SKBR3-derived EVs and MVs characterized by MS analysis. Most proteins showed non-significant differences in abundance between the two vesicle types. Members of the EGFR family (EGFR, HER2 and HER3) and SUSD2 are highlighted in red (More details in Supplementary Figure S2 b-f).

cryo-ET can be applied to both vesicle preparations (Fig. 1b and c). In this investigation, we acquired 35 and 36 tomograms from EVs and MVs respectively. Subsequent inspection of the tomograms indicated variability and heterogeneity in the physical appearance of the vesicles. Examples of x-y slices through tomograms of EVs are shown in Fig. 1d. Based on their morphology, we classified 92 EVs into 9 groups: (i) low inner-density vesicles (4%), (ii) elongated vesicles (3.0%), (iii) dense vesicles (9.0%), (iv) partially dense vesicles (22%), (v) cytoskeleton containing vesicles (13.0%), (vi) vesicles with droplet-like structures (droplets vesicles, 2.0%), (vii) multi-vesicular vesicles (multilamellar vesicles) (3.0%), (viii) crosslinked vesicles (4.0%), and (ix) others (40.0%) (Fig. 1e, left).

The MVs showed a similar appearance to the EVs; in total, we analyzed 98 MVs and classified them using the same morphological classification criteria as for the EVs (Fig. 1e right). Cryo-ET analysis of MVs indicated electron densities emanating from the membrane, many of these likely represent receptors (Fig. 1f white arrowheads). Our classification indicated that 77.5% of the MVs appear round and lack substantial internal densities (Fig. 1e, right), resembling the low inner-density EVs, which suggests that MVs are morphologically more homogeneous than EVs. In addition, the diameters of MVs and EVs are comparable, although MVs show lower variance in their diameters (Fig. 1g).

To gain insight into the protein composition of the EVs and the MVs, we performed a mass spectrometry-based proteome analysis of the two different vesicle types using a newly developed protocol for analysis of low sample loads (Ye et al., 2024). This analysis led to quantification of 6423 proteins from MVs and 6607 proteins from EVs (averages of 3 biological replicates). Among these proteins, 2375 proteins showed differential abundance between the two vesicle types (Fig. 1h and Fig. S2). Closer inspection of the two vesicle types indicated that the EVs are richer in cytoskeletal proteins, Rab proteins and exosomal proteins, whilst the MVs are richer in ribosomal proteins and proteins from the proteasome complex (Fig. S2). This could also be observed in cryo-EM images (see below).

Next, we applied the DeepLoc algorithm to predict the subcellular location of the identified proteins. The DeepLoc algorithm uses machine learning to predict the subcellular location of human proteins based on the protein's amino acid sequence (Almagro Armenteros et al., 2017). This analysis enabled us to predict which of the identified proteins that would locate into either the cell plasma membrane, organelles, nucleus or, if the proteins would be secreted. Focusing on the 10% most abundant proteins indicated that the diversity of membrane proteins is higher in the EVs than in the MVs (Fig. S2b). HER2 showed slightly higher abundance in EVs compared to MVs. In MVs, we detected similar levels of SUSD2 as of HER2.

We also used proteomaps (Liebermeister et al., 2014) to visualize the proteome compositions of the two different vesicles preparations. It is noteworthy that MVs have a higher content of ribosomal proteins, proteasome-related proteins, and proteins involved in glycolysis compared to EVs (Fig. S2h and i). The latter, however, showed higher abundance of cytoskeletal proteins and of proteins involved in signaling pathways. The observed proteome differences are attributable to the distinction between the pathway leading to EVs and the mechanical treatment of cells during the production of MVs(Banerjee et al., 2023; Tkach and Thery, 2016; van Niel et al., 2018; Goh et al., 2017; Jang et al., 2013; Lau et al., 2022).

The comparison of the protein composition between EVs and MVs revealed a substantial discrepancy in their protein composition, although the HER2 protein levels are similar in both SKBR3-derived EVs and MVs. Next, we proceeded to characterize the membrane protein composition, focusing exclusively on proteins containing signal peptides and transmembrane domains. This analysis demonstrated that HER2 is a highly abundant membrane protein in both MVs and EVs. However, EVs exhibit slightly greater morphological and compositional heterogeneity compared to MVs, and have higher inner-density, which is less favourable for cryo-EM based structural analysis.

3.2. A general method for the purification of HER2-containing vesicles

During the production of MVs the membrane curvature may become inverted. This results in a reversed orientation of the receptors, termed "outside-in" instead of the native "outside-out" receptor orientation. Therefore, we developed an affinity enrichment strategy based on DARPins (Pluckthun, 2015) immobilized on magnetic beads. Here, we took advantage of the DARPin G3, a previously developed HER2 binder that has a picomolar affinity to the extracellular domain (ECD) of HER2 (Jost et al., 2013; Zahnd et al., 2007), and could be equipped with a C-terminal protease cleavage site, followed by a C-terminal Avi-tag.

A key advantage of the applied enrichment strategy is that both the native and the inverse orientation of HER2-containing vesicles can in principle be obtained, using DARPins that target the extracellular or intracellular receptor domains, respectively. However, in this study, we only used the DARPin G3 that binds to subdomain IV of HER2 ECD (Cho et al., 2003). The flexible attachment of this

subdomain relative to subdomains I to III (Vacca et al., 2025) allows the binding to the DARPin G3 even to surfaces or bead.

The process involved three major steps (Fig. 2a): (1) streptavidin-coated magnetic beads were incubated with the biotin-conjugated DARPin G3 to produce G3-decorated magnetic beads; (2) binding of the HER2-containing vesicles to the DARPin G3-coated beads after mixing; (3) elution of the HER2-containing vesicles by proteolytic cleavage and release, followed by analysis by mass spectrometry and cryo-EM.

The optimal conditions for binding biotinylated DARPin G3 to streptavidin/coated magnetic beads and its subsequent release by 3C protease cleavage were validated by SDS-PAGE analysis (Fig. S3). More than 50% of the G3 protein was biotinylated, as indicated by the higher molecular weight band (lane 2, at approximately 65 kDa) when forming an SDS-PAGE/resistant complex with streptavidin. However, this shift was completely abolished following treatment with 3C protease, which cleaves off the biotinylated Avi-tag (lane 4, Fig. S3). Since unbiotinylated G3 cannot bind to streptavidin beads, an additional washing step after incubation ensures that unbound DARPins cannot interfere with the purification strategy. The feasibility of the approach was also validated using intact cells with and without HER2 expression (Fig. S4).

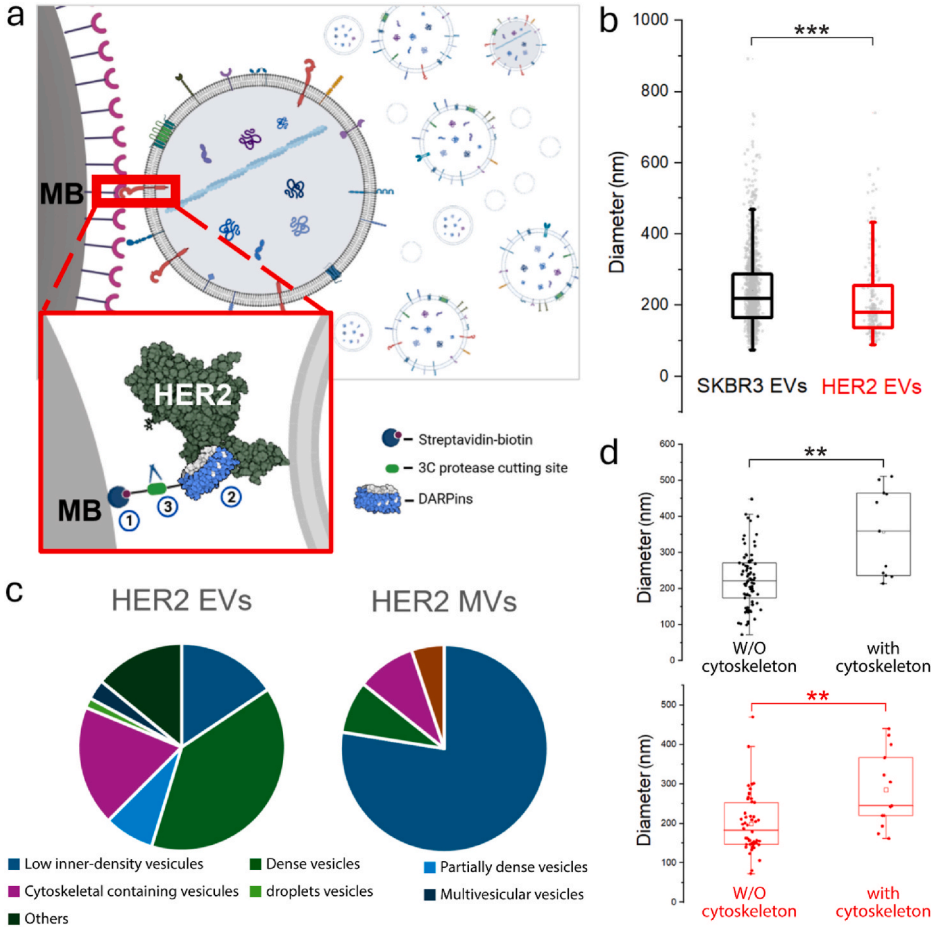

Fig. 2. HER2-containing vesicles purified by magnetic beads coated with protease-cleavable DARPins. a. Schematic illustration of our approach towards affinity enrichment of HER2-containing vesicles. Biotinylated DARPins with affinity to HER2 were immobilized on streptavidin-coated magnetic beads (MB) ①. The biotinylation site is located on an Avi-tag, separated from the DARPin by a 3C protease cleavage site. ② Vesicle bound to the DARPin-coated bead via the HER2 ECD. ③ Using 3C protease, the immobilized HER2-containing vesicles were released. **b.** Enriched HER2-containing EVs showed a reduced diameter in comparison to non-enriched EVs. The diameter was 190 ± 100 nm and 204 ± 100 nm for HER2-enriched EVs and EVs, respectively (average values are indicated by horizontal line, and the box range is from 25 to 75% of the whole population. **c.** The class distribution of EVs and MVs are displayed as a pie diagram. The enrichment approach influences the distribution of types of EVs more substantially than for MVs (cf. Fig. 1e). **d.** Size of EVs with (right) or without (left) cytoskeletal structures before (Upper panel) and after (Lower panel) HER2-based affinity purification, indicating the reduced size of the EVs independent of their content of cytoskeletal structures. MVs and HER2 MVs show no differences (data not shown). **b,d.** Box-and-whisker plots were generated using the Tukey method. Boxes represent the interquartile range (25th–75th percentiles), the horizontal line indicates the median, and the cross shows the mean. Whiskers extend to the most extreme values within 1.5 times the interquartile range; values beyond this range are shown as individual outliers. Statistical significance was assessed using the Welch's *t*-test. The p values for b and d, *** = 0.0006, ** = 0.0049 for SKBR* and ** = 0.0086 for HER2 EVs.

3.3. Characterization of HER2-containing EVs and MVs

HER2-containing EVs and MVs were enriched using the strategy described above followed by cryo-ET analysis. The average diameter of HER2-containing EVs was found to be 190 ± 100 nm, only slightly smaller than the average of the total population of EVs (Fig. 2b). Nevertheless, the difference in diameter was statistically significant. Next, we classified the enriched HER2-vesicles by their morphological characteristics, as done for the total EVs (Fig. 1d and e). Notably, two vesicle classes observed in EVs (Fig. 1e) were absent from the HER2-enriched EVs (Fig. 2c): t elongated vesicles and crosslinked vesicles. In contrast, the proportion of dense vesicles increased from 8.8% of EVs to 39.1% of HER2-enriched EVs (Fig. 2c). Additional notable changes were that cytoskeleton-containing and low density EVs were more frequent in HER2-enriched EVs (Fig. 2d). A possible explanation is that the length of the cytoskeletal elements favors their incorporation into larger vesicles, which were underrepresented in the HER2-enriched fraction.

These substantial variations between HER2-enriched vesicles and the total EV population were not found in MVs. This may be because a major determinant of their size is their mechanical isolation protocol which includes centrifugation steps, and is therefore less impacted by HER2 enrichment. Therefore, the morphological distribution of HER2-enriched MVs remained similar to the total population of SKBR3 MVs, with the low-density vesicles remaining the most abundant morphological class, accounting for over 70% of the vesicles in these samples (Fig. 2c).

Thus, significant differences were observed in the vesicle distribution both size-wise and morphologically between the naturally

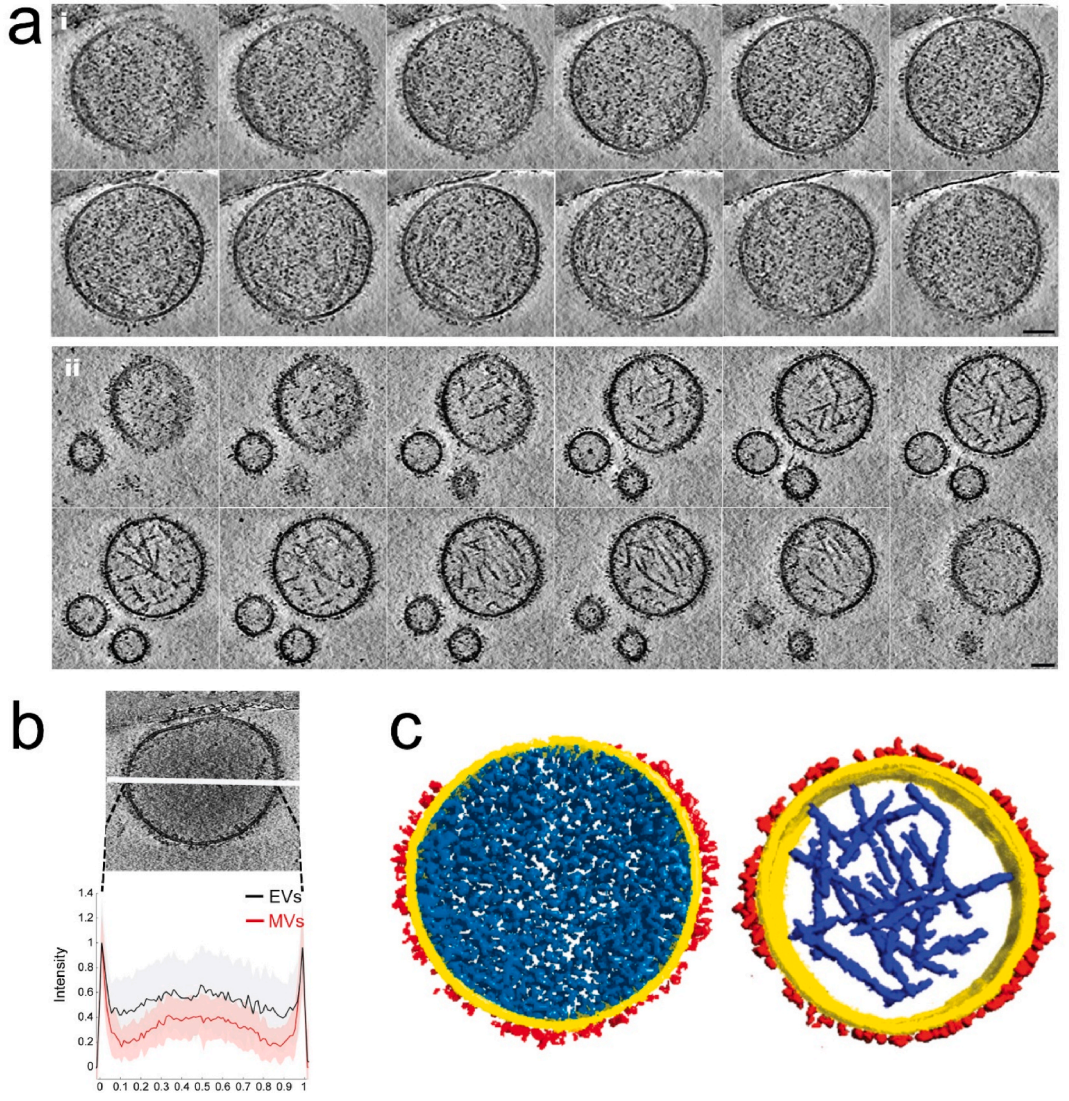

Fig. 3. HER2-containing EVs and MVs. a. x-y tomographic slices through a representative HER2-containing EV (i) and MV (ii). Scale bars are 100 nm. **b.** A white line through a vesicle (top) indicating the position of which the normalized intensity through HER2-containing EVs and MVs was drawn and analyzed (bottom). The standard deviation is shown by the shadowed area. **c.** The HER2-enriched EV (left) and MV (right) are shown as rendered views. Membrane (yellow), receptors (red), cytoskeleton (blue) and molecular structures (cyan).

occurring EVs and the mechanically induced MVs. For example, low inner-density vesicles accounted for only 15.6% of HER2-enriched EVs, compared with 70.2% of HER2-enriched MVs. Accordingly, this resulted in a higher average inner-density in HER2-enriched EVs compared to MVs (Fig. 2c), suggesting that EVs encapsulate a greater number of macromolecules. These differences imply that the release of EVs is not a random cellular process and that their structural characteristics may reflect specific biological functions (Bebelman et al., 2021).

3.4. Initial structure determination in native membranes

In many previous cases, structures of single transmembrane (TM) helix receptors were determined separately for their extracellular and the intracellular domains. However, this approach does not allow full visualization of the interaction with neighboring receptors in the same membrane, the effect of interacting proteins, e.g. therapeutic antibodies, or the impact of small molecules on the conformation of the receptor *in situ*. We therefore set out to develop strategies to allow structure determination of single-pass transmembrane receptors as full-length proteins in their natural environment. This is challenging due to EGFR family of receptors exhibiting several degrees of flexibility, even if dimerized (Arkhipov et al., 2013). The HER2 receptor contains a flexible linker between the single TM helix and its ectodomain, allowing it to adopt different orientations relative to the plasma membrane (Bragin et al., 2016). Furthermore, the different subdomains making up the extracellular domain can orient differently relative to each other. For example, even when purified, several conformations of the HER2 receptor have been detected, in addition to a spectrum of less abundant conformations (Vacca et al., 2025).

Many different membrane proteins are expected to be found in the membrane of cell derived vesicles, which was confirmed by our MS analysis (Table 1). This analysis showed that several proteins with similar molecular weights to that of HER2 are present in significant amounts and therefore may be misidentified as HER2 receptors in the initial identification of protein complexes in cryo-EM and cryo-ET. This is due to classification mostly depending on low-resolution information, defined by the size and the shape of the receptors. It is therefore extremely challenging to ensure 2D and 3D classes are constructed by averaging just a single type of membrane protein, which is essential for the structure determination of the targeted receptor residing in the native membrane.

As expected, cryo-ET analysis of HER2-containing EVs and MVs revealed a high number of proteins with similar dimensions as HER2 (Fig. 3a and b). In the tomograms the contrast was better for MVs than EVs, likely a result of the lower intravesicular density of the MVs (Fig. 3b and c). Although SKBR3 cells are known to natively express very high levels of HER2 receptors, the densely packed plasma membrane of the cells highlights the complexity of native membranes and the diversity of proteins embedded in them. Thus, the high density of proteins on the surface of MVs indicated another challenge which comes from the fact that HER2 receptors are localized in close proximity to many other proteins and may interact with additional membrane proteins in their native environment.

While sub-tomogram averaging (Briggs, 2013) may potentially be used to determine structures in the isolated vesicles, this method so far showed only limited success in resolving structures of receptors embedded in plasma membranes (Sorrentino et al., 2021). In contrast, high-resolution structures of ion channels have been resolved from cell-derived membrane vesicles (Tao et al., 2023). Importantly, the resolved structures were very homogeneous, likely due to the rigidity of the membrane-embedded part of these proteins. Furthermore, they have molecular weights more than twice that of the HER2 receptor (138 kDa). Nonetheless, these results suggest that cryo-EM could potentially be the method of choice for determining the structure of receptors embedded in MVs. To test

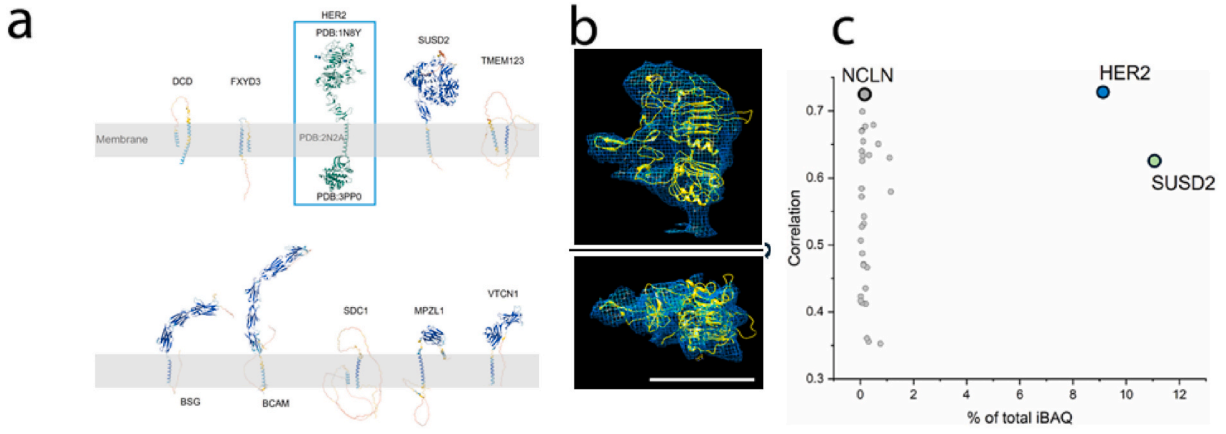

Fig. 4. Structure determination of receptors from SKBR3-derived MVs. a. The most abundant membrane proteins (by mass spectrometry analysis) in MVs were modelled using AlphaFold2, indicating that most of the abundant proteins are structurally distinguishable from HER2. **b.** The HER2 structure docked into the calculated 3D structure. The threshold of the structure was increased to also include the more flexible features. The structural subdomains of I, II and III of HER2 ECD were used for the docking. Scale bar 5 nm **c.** Visualization of the structural correlations between 34 membrane proteins, with comparably sized non-membrane domains to HER2, with the resulting 3D density map for HER2 as a function of the estimated protein abundance (total iBAQ). While HER2 showed the highest correlation, the ER protein NCLN showed a similar correlation value, however this membrane protein is found only in limited amounts. The protein SUSD2 appeared in a similar—lower though—abundance compared to HER2, but it showed only a correlation of 0.62, much lower than the reconstructed structure (see structural comparison in Fig. S8e).

this hypothesis, more than 10,000 micrographs were collected from SKBR3-derived MV samples. The high image quality of these rather thick specimens was validated by determining the structure of ribosomes present in the samples. Indeed, a well-resolved ribosome structure was obtained at 2.8 Å resolution (Fig. S5), confirming that the dataset contained sufficient high-resolution information for structural analysis.

To address the expected diversity of proteins included in our data from the analyzed particles, we first analyzed what the mass spectrometry results indicated as the most abundant membrane proteins in MVs using AlphaFold (Jumper et al., 2021) (Fig. 4a). We found that HER2 was the only abundant membrane protein with both extracellular and intracellular domains that would be large enough to be detected in cryo-EM micrographs. Furthermore, based on a previous structure of HER2, we expected that the HER2 extracellular domain (ECD) would extend approximately 10 nm away from the membrane, while the HER2 intracellular domain (ICD) would extend approximately 3 nm away from the membrane (PDB:1N8Z, 3PP0) (Aertgeerts et al., 2011). However, these distances may vary due to the conformational heterogeneity of HER2, full-length HER2 is inherently flexible. Notably, it is flexible at the hinges which connec the transmembrane helix to the extracellular and intracellular domains outside the membrane (Bragin et al., 2016).

Therefore, we adopted an image processing workflow that was guided by prior structural knowledge, i.e., the domain organization of HER2. After identification of all vesicles in our dataset, using the distinctly detectable lipid bilayer as a template (Fig. S6a), all electron densities emanating from the membrane were picked using a Topaz (Bepler et al., 2020) model trained on manually labeled examples. False positives, primarily located at carbon edges or inside vesicles, were removed based on the absence of bilayer structural features (Fig. S6b and c). Additional filtering of falsely picked densities was achieved by applying the expected dimensions of the HER2 ECD and ICD as selection criteria. Finally, initial 2D classification was performed to exclude densities smaller than 5 nm in diameter, which are unlikely to correspond to the HER2 ECD (Fig. S6d and e).

This procedure resulted in 151,480 particles with substantial densities emanating from the membrane. Next, we only analyzed the ICDs that are in close proximity to an ECD, although their relative positions may not be fixed given the expected flexibility of the cytoplasmic region of the HER2 receptor, both regarding rotation and position. To classify the ICD independently, the coordinates of each particle were shifted to the inner side of the membrane, and the particles were re-extracted then subjected to several rounds of 2D classification. All classes that displayed potential ICD densities were selected, which resulted in 55,760 particles (Fig. S6f and g). These particles were used to reconstruct a 3D map to modest resolution, which was subsequently used as template for 3D classification performed in RELION (Scheres, 2012), selecting ~50% of the particles as HER2 receptor candidates (Fig. S6h). This resulted in a structure resolved to 8.7 Å (Fig. 4b).

To analyze this structure, HER2 ECD subdomains I-III was fitted into the cryo-EM map using the Phenix package (Adams et al., 2010) (Fig. 4b). Although HER2 has not previously been determined within its native membrane, it is well accepted that subdomains I-III of its ECD are structurally rigid (Vacca et al., 2025). Therefore, a model consisting of HER2 subdomains I-III was used for fitting. The reconstructed structure clearly resembles the shape and size of the HER2 ECD resolved to <9 Å (Fig. S7). However, the refined structure did not show a clear ICD structure (Fig. S7). Similarly, in the structural analysis of purified quasi-full-length HER2, the flexibility in orientation of the ICD also prevented its structural determination, except at very modest resolution (Vacca et al., 2025). Interestingly, several structural classes obtained in the present analysis of densities extracted from the vesicles resemble a dimeric assembly of EGFR family receptors (Fig. S8). However, the limited number of detected structures in this conformation prevented the 3D reconstruction of these potential receptors dimers.

To further validate and provide additional insight into the densities observed at the SKBR3 membrane surface, we analyzed structures predicted with AlphaFold2 (Jumper et al., 2021) for all high abundance membrane proteins detected by mass spectroscopy and compared them with the reconstructed density maps. The proteins were then systematically classified into six groups according to their abundance and structural characteristics (Fig. S8c and Table 1). Five of these six groups were excluded as potential sources of densities that could be misidentified as HER2, as described below. (i) Low-abundance proteins: proteins that represent <0.01% of the total membrane protein content. This group of proteins was excluded from further analysis, because the low copy number (estimated as Intensity-Based Absolute Quantification, iBAQ, values from the MS data) reduces the probability that these proteins represent a large enough population to be reconstructed. (ii) proteins with large extra-cellular membrane domains. This group of membrane proteins contains ECDs larger than 1000 amino acids, which were excluded due to the incompatibility with the reconstructed map. (iii) Likewise, proteins with small ECD domains (<450 amino acids) were also excluded from further analysis. (iv) Proteins with tandem repeat domains which includes 26 membrane proteins. Most of which are involved in cell adhesion or intercellular junctions and have a unique structural feature which differs clearly from our map. Moreover, similar structures were observed in tomograms, where vesicles are crosslinked with each other (Fig. S8d). (v) Disordered proteins are those where the AlphaFold2 (Jumper et al., 2021) predictions for these 13 membrane proteins were too disordered to allow meaningful comparisons.

After excluding the proteins from the five groups, 34 membrane proteins that could be misinterpreted as HER2 remained (Supp. Table 1, bottom). Therefore, we downloaded their full length AlphaFold2 (Jumper et al., 2021) structures and trimmed their flexible domains based on the pLDDT confidence score. We then calculated the correlation coefficients (CC) for each structure with our reconstructed HER2 density map, using UCSF Chimera (Pettersen et al., 2004). Here, subdomains I-III of the HER2 ECD showed the highest CC value (CC = 0.724) with the derived structure followed by the ER protein NCLN (CC = 0.720), which is present at very low abundance (by iBAQ value estimation). In contrast, a plasma membrane protein with comparable abundance to HER2 showed a significantly lower CC value (CC = 0.623). These results support the validity of the workflow but cannot exclude the possibility that some included electron densities may originate from electron densities of other protein species, such as NCLN and SUSD2. Since the extracellular domain of the highly abundant SUSD2 does not fit well into the reconstructed density (Fig. S8e), it is likely that the majority of the density was contributed by the highly expressed HER2, and hence, that it is the HER2 receptor that was reconstructed from the native plasma membrane of cell-derived MVs, although at modest resolution.

4. Discussion

In the work presented, we assessed the suitability of different vesicle types derived from SKBR3 cells for the structural determination of HER2, which is highly expressed in SKBR3 cells. Naturally shed EVs offer a promising experimental system for studying receptors in vesicles, particularly due to the relatively high levels of HER2 receptors present in these vesicles. However, the EVs released by SKBR3 cells appeared to be heterogeneous in size and exhibited a relatively dense appearance in cryo-EM analysis. The differences in intravesicular densitiy observed between EVs and MVs may be the result of the mechanism of vesicle formation. EVs are formed from membrane evaginations caused by forces generated by cytoplasmic machinery on the plasma membrane. Whereas MVs are formed by passing cells through constricted volume. For MVs prepared from SKBR3 cells, the latter renders the sample more electron-transparent, which is a prerequisite for high-resolution cryo-EM and tomography analysis. Nevertheless, given the elevated HER2 expression levels, this system may also offer advantages for biochemical applications, such as measurements of the binding affinity of protein ligands, despite being less suited to structural investigations.

In contrast, our findings showed that mechanically induced vesicles (MVs), exhibit greater homogeneity in terms of morphology and size distribution, compared to EVs, while the expression levels of HER2 were found to be similar. Cryo-ET analysis highlighted the distinctive features of these vesicle preparations. However, the sub-tomogram averaging procedures did not yield a satisfactory reconstructed 3D structure of HER2. This was presumably due to the relatively low molecular weight of the HER2 receptor (<200 kDa), its orientational flexibility, the high contrast of the membrane, and the low signal-to-noise ratio of the tomograms. The application of cryo-ET to individual proteins, such as HER2, would facilitate the attainment of a more reliable 3D classification, allowing the identification of the complexes under scrutiny. Consequently, the image processing workflow employed in this study focuses on MVs using single particle analysis (SPA) for structural analysis.

Recently, several approaches have been developed to address heterogeneity in SPA, which demonstrated efficacy for purified protein complexes (Herreros et al., 2025; Schwab et al., 2024). Previous studies have also examined the application of cryo-EM for analysis of purified vesicles with overexpressed membrane proteins, focusing on proteins with rigid transmembrane regions. However, several challenges become apparent when the methods are applied to receptors with single transmembrane helices, which ultimately compromise the precision of the analysis when vesicles derived from native membranes are used. The primary challenge is the presence of a numerous other membrane proteins in native MVs, in addition to the protein of interest, as evidenced by MS analysis. This results in a diverse array of membrane proteins that are picked for the classification and subsequent analysis. Consequently, the selected particles likely included other membrane proteins with similar low-resolution structural features. This could not be overcome despite the utilization of prior knowledge, such as filtering based on predicted structural models of HER2 and of the other highly abundant membrane proteins present in the sample. Nonetheless, the approach facilitated a further computational enrichment of HER2 receptors in the particle picking step. In this regard, the development of cryo-EM labeling systems (Fung et al., 2023; Silvester et al., 2021) may facilitate circumventing this limitation in subsequent studies and are to be investigated.

An inherent challenge in the structural studies of single-pass transmembrane-helix receptors like HER2 is the variability in ECD orientation. This flexibility of the angle between subdomain IV and the transmembrane helix has also been demonstrated previously for other EGFR-related proteins (Arkhipov et al., 2013; Huang et al., 2021; Vacca et al., 2025). A challenge of both vesicle preparations is the relativey large size of the vesicles for use as cryo-EM specimens. The mean diameter of the vesicles exceeds 150 nm, thereby leading to increased ice thickness. In comparison, high-resolution structures of the ion channel Slo1 were resolved from vesicles with a diameter of approximately 40 nm (Tao et al., 2023), a size obtained by sonication. Thicker ice results in a reduced signal-to-noise ratio in the acquired micrographs, which directly impacts the resolution of the resulting structures. Despite thicker ice, the samples permitted determination of ribosome structures at high resolution (Fig. S5). However, the reconstruction of small and more fragile elements remains challenging.

Although the resolution of our reconstructed structure was insufficient to produce a high-resolution density map of HER2, a thorough comparison with other proteins in our sample strongly suggested that the reconstructed structure corresponded to the receptor. Although a high-resolution structure of HER2 could not be derived, the approach followed suggests that a human breast cancer cell line like SKBR3 has potential for use instructural analysis. The ICD of HER2 becomes much less resolved after reconstruction, which indicates high flexibility between the ECD and ICD of HER2 with native membranes, as found in previous studies (Campbell et al., 2022; Vacca et al., 2025). Nonetheless, a dedicated averaging of micrographs focusing on this domain independently of the ECD may help to gain further information in these structural features.

In summary, the present study reports the differences between EVs and MVs for structural studies, thereby evaluating the applicability of these preparations as specimens for *in situ* membrane protein structural analysis. Future advances in cryo-EM and cryo-ET, together with developments in labelling technologies, are expected to further improve the high-resolution structural analysis of HER2 in its native environment. Such technological advances have the potential to enable the reconstruction of individual transmembrane receptors within cellular contexts.

CRediT authorship contribution statement

Chunyang Wang: Writing – original draft, Visualization, Validation, Methodology, Formal analysis, Data curation. **Ole Østergaard:** Writing – original draft, Validation, Methodology, Investigation, Formal analysis, Data curation. **Roberto Melero:** Writing – review & editing, Methodology, Formal analysis. **Gabriela Nagy-Davidescu:** Methodology. **Matthias Eibauer:** Writing – review & editing, Writing – original draft, Supervision, Project administration. **Jesper Velgaard Olsen:** Supervision, Funding acquisition. **Jose Maria Carazo:** Writing – review & editing, Supervision, Funding acquisition. **Andreas Plückthun:** Writing – review

& editing, Writing – original draft, Supervision, Funding acquisition, Conceptualization. **Ohad Medalia:** Writing – review & editing, Writing – original draft, Supervision, Funding acquisition, Conceptualization.

Declaration of competing interest

The authors declare that they have no known competing financial interests or personal relationships that could have appeared to influence the work reported in this paper.The author is an Editorial Board Member/Editor-in-Chief/Associate Editor/Guest Editor for this journal and was not involved in the editorial review or the decision to publish this article.

Acknowledgements

Imaging was performed with equipment maintained by the Center for Microscopy and Image Analysis (ZMB), University of Zürich. We thank R. Boujemaa-Paterski for helping with the artwork. This work was supported by the European Research Council grant HighResCells (ERC-2018-SyG, proposal: 810057 to J.O, J.M.C. A.P., and O.M.).

Appendix A. Supplementary data

Supplementary data to this article can be found online at https://doi.org/10.1016/j.jbior.2026.101191.

Data availability

The recorded mass spectrometry RAW files along with the search result has been uploaded to the data repository PRIDE (Perez-Riverol et al., 2025)and are accessible with the following identifier: PXD074163.

The output from Spectronaut were analyzed further using Rstudio (v2022.12 B353, R version 4.2.2). Proteomaps (Liebermeister et al., 2014) were used to visualize the quantitative composition of selected samples.

Represented tomograms of EVs EMD-53710, MVs EMD-53712, and the structure of membrane protein in Fig. 4b, EMD-55738.

References

Adams, P.D., Afonine, P.V., Bunkoczi, G., Chen, V.B., Davis, I.W., Echols, N., Headd, J.J., Hung, L.W., Kapral, G.J., Grosse-Kunstleve, R.W., McCoy, A.J., Moriarty, N. W., Oeffner, R., Read, R.J., Richardson, D.C., Richardson, J.S., Terwilliger, T.C., Zwart, P.H., 2010. PHENIX: a comprehensive Python-based system for macromolecular structure solution. Acta Crystallogr. D Biol. Crystallogr. 66 (Pt 2), 213–221.

Aertgeerts, K., Skene, R., Yano, J., Sang, B.C., Zou, H., Snell, G., Jennings, A., Iwamoto, K., Habuka, N., Hirokawa, A., Ishikawa, T., Tanaka, T., Miki, H., Ohta, Y., Sogabe, S., 2011. Structural analysis of the mechanism of inhibition and allosteric activation of the kinase domain of HER2 protein. J. Biol. Chem. 286 (21), 18756–18765.

Almagro Armenteros, J.J., Sonderby, C.K., Sonderby, S.K., Nielsen, H., Winther, O., 2017. DeepLoc: prediction of protein subcellular localization using deep learning. Bioinformatics 33 (24), 4049.

Arkhipov, A., Shan, Y., Das, R., Endres, N.F., Eastwood, M.P., Wemmer, D.E., Kuriyan, J., Shaw, D.E., 2013. Architecture and membrane interactions of the EGF receptor. Cell 152 (3), 557–569.

Asarnow, D., Palovcak, E., Cheng, Y., 2019. UCSF Pyem v0. 5. Zenodo 3576630.

Banerjee, A., Lino, M., Jesus, C., Ribeiro, Q., Abrunhosa, A., Ferreira, L., 2023. Imaging platforms to dissect the in vivo communication, biodistribution and controlled release of extracellular vesicles. J. Contr. Release 360, 549–563.

Bebelman, M.P., Janssen, E., Pegtel, D.M., Crudden, C., 2021. The forces driving cancer extracellular vesicle secretion. Neoplasia 23 (1), 149–157.

Bechara, C., Noll, A., Morgner, N., Degiacomi, M.T., Tampe, R., Robinson, C.V., 2015. A subset of annular lipids is linked to the flippase activity of an ABC transporter. Nat. Chem. 7 (3), 255–262.

Bepler, T., Kelley, K., Noble, A.J., Berger, B., 2020. Topaz-Denoise: general deep denoising models for cryoEM and cryoET. Nat. Commun. 11 (1), 5208.

Bhagyalalitha, M., Handattu Shankaranarayana, A., Arun Kumar, S., Singh, M., Pujar, K.G., Bidye, D., Veeranna Pujar, G., 2024. Advances in HER2-Targeted therapies: from monoclonal antibodies to dual inhibitors developments in cancer treatment. Bioorg. Chem. 151, 107695.

Bragin, P.E., Mineev, K.S., Bocharova, O.V., Volynsky, P.E., Bocharov, E.V., Arseniev, A.S., 2016. HER2 transmembrane domain dimerization coupled with self-association of membrane-embedded cytoplasmic juxtamembrane regions. J. Mol. Biol. 428 (1), 52–61.

Briggs, J.A., 2013. Structural biology in situ–the potential of subtomogram averaging. Curr. Opin. Struct. Biol. 23 (2), 261–267.

Campbell, M.R., Ruiz-Saenz, A., Zhang, Y., Peterson, E., Steri, V., Oeffinger, J., Sampang, M., Jura, N., Moasser, M.M., 2022. Extensive conformational and physical plasticity protects HER2-HER3 tumorigenic signaling. Cell Rep. 38 (5), 110285.

Cheng, X., Smith, J.C., 2019. Biological membrane organization and cellular signaling. Chem. Rev. 119 (9), 5849–5880.

Cho, H.S., Mason, K., Ramyar, K.X., Stanley, A.M., Gabelli, S.B., Denney Jr, D.W., Leahy, D.J., 2003. Structure of the extracellular region of HER2 alone and in complex with the Herceptin Fab. Nature 421 (6924), 753–760.

Chung, I., Reichelt, M., Shao, L., Akita, R.W., Koeppen, H., Rangell, L., Schaefer, G., Mellman, I., Sliwkowski, M.X., 2016. High cell-surface density of HER2 deforms cell membranes. Nat. Commun. 7, 12742.

Costa, R.L.B., Czerniecki, B.J., 2020. Clinical development of immunotherapies for HER2(+) breast cancer: a review of HER2-directed monoclonal antibodies and beyond. NPJ Breast Cancer 6, 10.

de la Rosa-Trevin, J.M., Quintana, A., Del Cano, L., Zaldivar, A., Foche, I., Gutierrez, J., Gomez-Blanco, J., Burguet-Castell, J., Cuenca-Alba, J., Abrishami, V., Vargas, J., Oton, J., Sharov, G., Vilas, J.L., Navas, J., Conesa, P., Kazemi, M., Marabini, R., Sorzano, C.O., Carazo, J.M., 2016. Scipion: a software framework toward integration, reproducibility and validation in 3D electron microscopy. J. Struct. Biol. 195 (1), 93–99.

Delauzun, V., Amigues, B., Gaubert, A., Leone, P., Grange, M., Gauthier, L., Roussel, A., 2020. Extracellular vesicles as a platform to study cell-surface membrane proteins. Methods 180, 35–44.

Denisov, I.G., Sligar, S.G., 2016. Nanodiscs for structural and functional studies of membrane proteins. Nat. Struct. Mol. Biol. 23 (6), 481–486.

Diamant, M., Tushuizen, M.E., Sturk, A., Nieuwland, R., 2004. Cellular microparticles: new players in the field of vascular disease? Eur. J. Clin. Invest. 34 (6), 392–401.

Englmeier, R., Pfeffer, S., Forster, F., 2017. Structure of the human mitochondrial ribosome studied in situ by Cryoelectron Tomography. Structure 25 (10), 1574–1581 e1572.
Fung, H.K.H., Hayashi, Y., Salo, V.T., Babenko, A., Zagoriy, I., Brunner, A., Ellenberg, J., Muller, C.W., Cuylen-Haering, S., Mahamid, J., 2023. Genetically encoded multimeric tags for subcellular protein localization in cryo-EM. Nat. Methods 20 (12), 1900–1908.
Goh, W.J., Zou, S., Ong, W.Y., Torta, F., Alexandra, A.F., Schiffelers, R.M., Storm, G., Wang, J.W., Czarny, B., Pastorin, G., 2017. Bioinspired cell-derived nanovesicles versus exosomes as drug delivery systems: a cost-effective alternative. Sci. Rep. 7 (1), 14322.
Gonzalez-Magaldi, M., Gullapalli, A., Papoulas, O., Liu, C., Leung, A.Y., Guo, L., Brilot, A.F., Marcotte, E.M., Ke, Z., Leahy, D.J., 2025. Structure and organization of full-length epidermal growth factor receptor in extracellular vesicles by cryo-electron tomography. Proc. Natl. Acad. Sci. U. S. A. 122 (23), e2424678122.
Graus-Porta, D., Beerli, R.R., Daly, J.M., Hynes, N.E., 1997. ErbB-2, the preferred heterodimerization partner of all ErbB receptors, is a mediator of lateral signaling. EMBO J. 16 (7), 1647–1655.
Han, T.W., Ye, W., Bethel, N.P., Zubia, M., Kim, A., Li, K.H., Burlingame, A.L., Grabe, M., Jan, Y.N., Jan, L.Y., 2019. Chemically induced vesiculation as a platform for studying TMEM16F activity. Proc. Natl. Acad. Sci. U. S. A 116 (4), 1309–1318.
Harapin, J., Bormel, M., Sapra, K.T., Brunner, D., Kaech, A., Medalia, O., 2015. Structural analysis of multicellular organisms with cryo-electron tomography. Nat. Methods 12 (7), 634–636.
Harayama, T., Riezman, H., 2018. Understanding the diversity of membrane lipid composition. Nat. Rev. Mol. Cell Biol. 19 (5), 281–296.
Herreros, D., Mata, C.P., Noddings, C., Irene, D., Krieger, J., Agard, D.A., Tsai, M.D., Sorzano, C.O.S., Carazo, J.M., 2025. Real-space heterogeneous reconstruction, refinement, and disentanglement of CryoEM conformational states with HetSIREN. Nat. Commun. 16 (1), 3751.
Huang, Y., Ognjenovic, J., Karandur, D., Miller, K., Merk, A., Subramaniam, S., Kuriyan, J., 2021. A molecular mechanism for the generation of ligand-dependent differential outputs by the epidermal growth factor receptor. eLife 10, e73218.
Jang, S.C., Kim, O.Y., Yoon, C.M., Choi, D.S., Roh, T.Y., Park, J., Nilsson, J., Lotvall, J., Kim, Y.K., Gho, Y.S., 2013. Bioinspired exosome-mimetic nanovesicles for targeted delivery of chemotherapeutics to malignant tumors. ACS Nano 7 (9), 7698–7710.
Jost, C., Schilling, J., Tamaskovic, R., Schwill, M., Honegger, A., Pluckthun, A., 2013. Structural basis for eliciting a cytotoxic effect in HER2-overexpressing cancer cells via binding to the extracellular domain of HER2. Structure 21 (11), 1979–1991.
Jumper, J., Evans, R., Pritzel, A., Green, T., Figurnov, M., Ronneberger, O., Tunyasuvunakool, K., Bates, R., Zidek, A., Potapenko, A., Bridgland, A., Meyer, C., Kohl, S. A.A., Ballard, A.J., Cowie, A., Romera-Paredes, B., Nikolov, S., Jain, R., Adler, J., Back, T., Petersen, S., Reiman, D., Clancy, E., Zielinski, M., Steinegger, M., Pacholska, M., Berghammer, T., Bodenstein, S., Silver, D., Vinyals, O., Senior, A.W., Kavukcuoglu, K., Kohli, P., Hassabis, D., 2021. Highly accurate protein structure prediction with AlphaFold. Nature 596 (7873), 583–589.
Junttila, T.T., Akita, R.W., Parsons, K., Fields, C., Lewis Phillips, G.D., Friedman, L.S., Sampath, D., Sliwkowski, M.X., 2009. Ligand-independent HER2/HER3/PI3K complex is disrupted by trastuzumab and is effectively inhibited by the PI3K inhibitor GDC-0941. Cancer Cell 15 (5), 429–440.
Kalluri, R., McAndrews, K.M., 2023. The role of extracellular vesicles in cancer. Cell 186 (8), 1610–1626.
Kaplan, M., Narasimhan, S., de Heus, C., Mance, D., van Doorn, S., Houben, K., Popov-Celeketic, D., Damman, R., Katrukha, E.A., Jain, P., Geerts, W.J.C., Heck, A.J.R., Folkers, G.E., Kapitein, L.C., Lemeer, S., van Bergen En Henegouwen, P.M.P., Baldus, M., 2016. EGFR dynamics change during activation in native membranes as revealed by NMR. Cell 167 (5), 1241–1251 e1211.
Keller, J., Fernandez-Busnadiego, R., 2024. In situ studies of membrane biology by cryo-electron tomography. Curr. Opin. Cell Biol. 88, 102363.
Kesidis, A., Depping, P., Lode, A., Vaitsopoulou, A., Bill, R.M., Goddard, A.D., Rothnie, A.J., 2020. Expression of eukaryotic membrane proteins in eukaryotic and prokaryotic hosts. Methods 180, 3–18.
Kimanius, D., Jamali, K., Wilkinson, M.E., Lovestam, S., Velazhahan, V., Nakane, T., Scheres, S.H.W., 2024. Data-driven regularization lowers the size barrier of cryo-EM structure determination. Nat. Methods 21.
Kremer, J.R., Mastronarde, D.N., Mclntosh, J.R., 1996. Computer visualization of three-dimensional image data using IMOD. J. Struct. Biol. 116 (1), 71–76.
Lau, H.C., Han, D.W., Park, J., Lehner, E., Kals, C., Arzt, C., Bayer, E., Auer, D., Schally, T., Grasmann, E., Fang, H., Lee, J.Y., Lee, H.S., Han, J., Gimona, M., Rohde, E., Bae, S., Oh, S.W., 2022. GMP-compliant manufacturing of biologically active cell-derived vesicles produced by extrusion technology. J. Extracell Biol. 1 (12), e70.
Levental, I., Grzybek, M., Simons, K., 2011. Raft domains of variable properties and compositions in plasma membrane vesicles. Proc. Natl. Acad. Sci. U. S. A 108 (28), 11411–11416.
Levental, I., Lyman, E., 2023. Regulation of membrane protein structure and function by their lipid nano-environment. Nat. Rev. Mol. Cell Biol. 24 (2), 107–122.
Liebermeister, W., Noor, E., Flamholz, A., Davidi, D., Bernhardt, J., Milo, R., 2014. Visual account of protein investment in cellular functions. Proc. Natl. Acad. Sci. U. S. A 111 (23), 8488–8493.
Liu, C., Leighow, S.M., McIlroy, K., Lu, M., Dennis, K.A., Abello, K., Brown, D.J., Moore, C.J., Shah, A., Inam, H., Rivera, V.M., Pritchard, J.R., 2023. Excessive concentrations of kinase inhibitors in translational studies impede effective drug repurposing. Cell Rep. Med. 4 (10), 101227.
Mahamid, J., Pfeffer, S., Schaffer, M., Villa, E., Danev, R., Cuellar, L.K., Forster, F., Hyman, A.A., Plitzko, J.M., Baumeister, W., 2016. Visualizing the molecular sociology at the HeLa cell nuclear periphery. Science 351 (6276), 969–972.
Munguira, I., Casuso, I., Takahashi, H., Rico, F., Miyagi, A., Chami, M., Scheuring, S., 2016. Glasslike membrane protein diffusion in a crowded membrane. ACS Nano 10 (2), 2584–2590.
Nabholtz, J.M., Reese, D.M., Lindsay, M.A., Riva, A., 2002. HER2-positive breast cancer: update on Breast Cancer International Research Group trials. Clin. Breast Cancer 3 (Suppl. 2), S75–S79.
Nickell, S., Forster, F., Linaroudis, A., Net, W.D., Beck, F., Hegerl, R., Baumeister, W., Plitzko, J.M., 2005. TOM software toolbox: acquisition and analysis for electron tomography. J. Struct. Biol. 149 (3), 227–234.
Perez-Riverol, Y., Bandla, C., Kundu, D.J., Kamatchinathan, S., Bai, J., Hewapathirana, S., John, N.S., Prakash, A., Walzer, M., Wang, S., Vizcaino, J.A., 2025. The PRIDE database at 20 years: 2025 update. Nucleic Acids Res. 53 (D1), D543–D553.
Pettersen, E.F., Goddard, T.D., Huang, C.C., Couch, G.S., Greenblatt, D.M., Meng, E.C., Ferrin, T.E., 2004. UCSF Chimera–a visualization system for exploratory research and analysis. J. Comput. Chem. 25 (13), 1605–1612.
Pluckthun, A., 2015. Designed ankyrin repeat proteins (DARPins): binding proteins for research, diagnostics, and therapy. Annu. Rev. Pharmacol. Toxicol. 55, 489–511.
Punjani, A., Rubinstein, J.L., Fleet, D.J., Brubaker, M.A., 2017. cryoSPARC: algorithms for rapid unsupervised cryo-EM structure determination. Nat. Methods 14 (3), 290–296.
Rouck, J.E., Krapf, J.E., Roy, J., Huff, H.C., Das, A., 2017. Recent advances in nanodisc technology for membrane protein studies (2012-2017). FEBS Lett. 591 (14), 2057–2088.
Rubinstein, J.L., 2026. Cryo-EM of endogenous membrane proteins in their native lipid bilayer. Q. Rev. Biophys. 59, e3.
Saifudeen, M., Zhu, S., Liang, S., Eason, M., Goupil, A., Mische, D.F., Loch, C.M., Ma, H., Chan, M., Gujral, T.S., 2026. Comprehensive profiling of clinically approved kinase inhibitors reveals mutation-specific inhibitors and opportunities for drug repurposing. Nat. Biotechnol.
Salih, D.J., Reiners, K.S., Alfieri, R., Salih, A.M., Percario, Z.A., Di Stefano, M., Francesco, S., Affabris, E., Hartmann, G., Santantonio, T., 2025. Isolation and characterization of extracellular vesicles from EGFR mutated lung cancer cells. Clin. Exp. Med. 25 (1), 114.
Schaffer, M., Mahamid, J., Engel, B.D., Laugks, T., Baumeister, W., Plitzko, J.M., 2017. Optimized cryo-focused ion beam sample preparation aimed at in situ structural studies of membrane proteins. J. Struct. Biol. 197 (2), 73–82.
Scheres, S.H., 2012. RELION: implementation of a Bayesian approach to cryo-EM structure determination. J. Struct. Biol. 180 (3), 519–530.
Schmidtmann, M., D'Souza-Schorey, C., 2023. Extracellular vesicles: biological packages that modulate tumor cell invasion. Cancers (Basel) 15 (23).
Schuller, A.P., Wojtynek, M., Mankus, D., Tatli, M., Kronenberg-Tenga, R., Regmi, S.G., Dip, P.V., Lytton-Jean, A.K.R., Brignole, E.J., Dasso, M., Weis, K., Medalia, O., Schwartz, T.U., 2021. The cellular environment shapes the nuclear pore complex architecture. Nature 598 (7882), 667–671.
Schwab, J., Kimanius, D., Burt, A., Dendooven, T., Scheres, S.H.W., 2024. DynaMight: estimating molecular motions with improved reconstruction from cryo-EM images. Nat. Methods 21 (10), 1855–1862.

Shyam Sunder, S., Sharma, U.C., Pokharel, S., 2023. Adverse effects of tyrosine kinase inhibitors in cancer therapy: pathophysiology, mechanisms and clinical management. Signal Transduct. Targeted Ther. 8 (1), 262.

Silvester, E., Vollmer, B., Prazak, V., Vasishtan, D., Machala, E.A., Whittle, C., Black, S., Bath, J., Turberfield, A.J., Grunewald, K., Baker, L.A., 2021. DNA origami signposts for identifying proteins on cell membranes by electron cryotomography. Cell 184 (4), 1110–1121 e1116.

Sorrentino, S., Conesa, J.J., Cuervo, A., Melero, R., Martins, B., Fernandez-Gimenez, E., de Isidro-Gomez, F.P., de la Morena, J., Studt, J.D., Sorzano, C.O.S., Eibauer, M., Carazo, J.M., Medalia, O., 2021. Structural analysis of receptors and actin polarity in platelet protrusions. Proc. Natl. Acad. Sci. U. S. A. 118 (37).

Tao, X., Zhao, C., MacKinnon, R., 2023. Membrane protein isolation and structure determination in cell-derived membrane vesicles. Proc. Natl. Acad. Sci. U. S. A 120 (18), e2302325120.

Tkach, M., Thery, C., 2016. Communication by extracellular vesicles: where we are and where we need to Go. Cell 164 (6), 1226–1232.

Vacca, S., Gragera, M., Buschiazzo, A., Herreros, D., Krieger, J.M., Bonn-Garcia, S., Melero, R., Sorzano, C.O., Carazo, J.M., Medalia, O., Plückthun, A., 2025. Structural analysis of HER2-trastuzumab complex reveals receptor conformational adaptation. Sci. Adv. 11 (30), eadu9945.

van Niel, G., D'Angelo, G., Raposo, G., 2018. Shedding light on the cell biology of extracellular vesicles. Nat. Rev. Mol. Cell Biol. 19 (4), 213–228.

Vitrac, H., Bogdanov, M., Dowhan, W., 2013. In vitro reconstitution of lipid-dependent dual topology and postassembly topological switching of a membrane protein. Proc. Natl. Acad. Sci. U. S. A 110 (23), 9338–9343.

Yarden, Y., Sliwkowski, M.X., 2001. Untangling the ErbB signalling network. Nat. Rev. Mol. Cell Biol. 2 (2), 127–137.

Ye, Z., Sabatier, P., Martin-Gonzalez, J., Eguchi, A., Lechner, M., Ostergaard, O., Xie, J., Guo, Y., Schultz, L., Truffer, R., Bekker-Jensen, D.B., Bache, N., Olsen, J.V., 2024. One-Tip enables comprehensive proteome coverage in minimal cells and single zygotes. Nat. Commun. 15 (1), 2474.

Yu, J., Fang, T., Yun, C., Liu, X., Cai, X., 2022. Antibody-Drug conjugates targeting the human epidermal growth factor receptor family in cancers. Front. Mol. Biosci. 9, 847835.

Zahnd, C., Wyler, E., Schwenk, J.M., Steiner, D., Lawrence, M.C., McKern, N.M., Pecorari, F., Ward, C.W., Joos, T.O., Pluckthun, A., 2007. A designed ankyrin repeat protein evolved to picomolar affinity to Her2. J. Mol. Biol. 369 (4), 1015–1028.

Zeev-Ben-Mordehai, T., Vasishtan, D., Siebert, C.A., Whittle, C., Grunewald, K., 2014. Extracellular vesicles: a platform for the structure determination of membrane proteins by Cryo-EM. Structure 22 (11), 1687–1692.

Zimmerli, C.E., Allegretti, M., Rantos, V., Goetz, S.K., Obarska-Kosinska, A., Zagoriy, I., Halavatyi, A., Hummer, G., Mahamid, J., Kosinski, J., Beck, M., 2021. Nuclear pores dilate and constrict in cellulo. Science 374 (6573), eabd9776.